

## Article

# Preparation of Core–Shell Structure W/Gd<sub>2</sub>O<sub>3</sub> and Study on the Properties of Radiation Protection Materials

Yong Xia, Tao Yang, Gangwei Pan, Sijun Xu and Lirong Yao \*

National & Local Joint Engineering Research Center of Technical Fiber Composites for Safety and Protection, Nantong University, Nantong 226019, China; XiaYong1124@hotmail.com (Y.X.); r415901420@163.com (T.Y.); pangangwei@ntu.edu.cn (G.P.); xusijunwork@hotmail.com (S.X.)

\* Correspondence: ylr8231@ntu.edu.cn; Tel.: +86-15051262516

**Abstract:** W/Polydopamine (PDA) was prepared by adding W powder into the dopamine (DA) solution and adjusting the pH value of the solution. PDA contains several phenolic hydroxyl and amino groups, which provide abundant active sites for the complexation of metal ions. Therefore, we prepared W/Gd<sub>2</sub>O<sub>3</sub> with core–shell structure by self-assembly method and homogeneous precipitation method, respectively. At the same time, polyurethane (PU) coating fabrics with W and Gd<sub>2</sub>O<sub>3</sub> mixed powder and core–shell W/Gd<sub>2</sub>O<sub>3</sub> powder were prepared, and their X-ray protection performance was tested. Results show that compared with W and Gd<sub>2</sub>O<sub>3</sub> mixed powder PU coating fabrics, the protection efficiency and lead equivalent of core–shell structure W/Gd<sub>2</sub>O<sub>3</sub> powder PU coating fabrics against different energy rays are obviously improved. With the increase in incident energy, the protective efficiency of core–shell structure W/Gd<sub>2</sub>O<sub>3</sub> powder PU coating fabric decreases more slowly than that of W/Gd<sub>2</sub>O<sub>3</sub> mixed powder PU coating fabric. When the incident energy is 65–100 keV, the protective efficiency of the core–shell structure W/Gd<sub>2</sub>O<sub>3</sub> powder PU coating fabric is above 60%, showing a good synergistic protective effect. When the incident energy is 83 keV, the X-ray protection efficiency of core–shell W/Gd<sub>2</sub>O<sub>3</sub> powder PU coating fabric is 65.5%, and the lead equivalent is 0.4051 mmPb.



**Citation:** Xia, Y.; Yang, T.; Pan, G.; Xu, S.; Yao, L. Preparation of Core–Shell Structure W/Gd<sub>2</sub>O<sub>3</sub> and Study on the Properties of Radiation Protection Materials. *Coatings* **2022**, *12*, 851. <https://doi.org/10.3390/coatings12060851>

Academic Editor: Valentin Craciun

Received: 15 May 2022

Accepted: 14 June 2022

Published: 17 June 2022

**Publisher's Note:** MDPI stays neutral with regard to jurisdictional claims in published maps and institutional affiliations.



**Copyright:** © 2022 by the authors. Licensee MDPI, Basel, Switzerland. This article is an open access article distributed under the terms and conditions of the Creative Commons Attribution (CC BY) license (<https://creativecommons.org/licenses/by/4.0/>).

**Keywords:** X-ray protection; polydopamine; self-assembly method; homogeneous precipitation method; core–shell structure W/Gd<sub>2</sub>O<sub>3</sub>

## 1. Introduction

The development of nuclear technology brings convenience to people, but it also brings a lot of radiation hazards. Lightweight, flexible, and excellent protective textiles for radiation protection are the current research hotspots [1]. Radiation protection materials are mainly divided into lead-containing materials and lead-free materials. Lead-containing materials are mainly composed of lead, which has a good protective effect, but it is toxic, poor in strength, and poor in absorption efficiency of low-energy X-rays. Lead-free materials mainly include composite materials made of rare earth elements and heavy metal compounds such as tin (Sn), tungsten (W), and bismuth (Bi), which have excellent protection effects and are light and safe [2–6].

Nuñez et al. [7] prepared composite shielding materials by adding bismuth oxide into polyvinyl chloride. The results show that when the bismuth oxide content is 50 wt%, the X-ray transmittance at a voltage of 20–30 kV is almost zero, and the transmittance at 61 kV is 20%. Cherkashina et al. [8] used bismuth silicate as a filler for polyimide radiation shielding composite. The results show that when bismuth silicate is added at 50 wt%, the linear attenuation coefficient of the composite is 2.5 and 1.4 times that of aluminum at 0.5 and 1 MeV energies, respectively. Kijima et al. [9] prepared a new type of tungsten-containing rubber. The research shows that tungsten-containing rubber has good radiation shielding performance. When considering the half-value layer, half-life, energy, and activity

of tungsten-containing rubber, it is safe and effective in protecting radionuclides and can be used as a protective material in clinical sites.

Bilous et al. [10] studied the relationship between radiation protection efficiency and structure of Al-Pb multilayer composite and found that the radiation protection efficiency of Al-Pb composite was 30–40% higher than that of pure Al. Hoyeon et al. [11] prepared Bi-Sn/polymer/W composite material, tested it, and found that it can achieve the effect of synergistic protection. The 20 mm thick Bi-Sn/polymer/W composite material can achieve the complete attenuation of 667 keV gamma radiation from a  $^{137}\text{Cs}$  source.

A single metal or metal compound can only shield the energy in a certain range, and the use of multi-metal or metal compounds to prepare radiation-proof materials can play a synergistic role in the protection and eliminate the weak protection areas. Compared with the radiation-proof material prepared by physical blending, the radiation-proof material with core-shell structure [12] prepared by a certain method can effectively absorb the secondary radiation generated by radiation. The preparation methods of core-shell structure mainly include template method, precipitation method, hydrothermal synthesis method, spray drying method, and layer-by-layer self-assembly technology [13–17]. Yin et al. [18] prepared gadolinium-oxide-coated silica core-shell nanoparticles with highly uniform dispersion and controllable shell thickness by a homogeneous precipitation method. These nanoparticles are a new type of nuclear magnetic resonance contrast agent with high sensitivity and tumor-targeting ability. Li et al. [19] prepared gadolinium oxide hollow spheres with controllable shell thickness by homogeneous precipitation method using silica as a template.

The adhesive protein secreted by mussels has a strong adhesive ability. Inspired by this, Messer et al. of Northwestern University discovered in 2007 that dopamine (DA) could be oxidized and self-polymerized on the surface of any material under the weak alkaline condition of simulated seawater to form polydopamine (PDA) [20]. Its polymerization conditions are simple and controllable, and it has excellent adhesion, hydrophilicity, stability, and biocompatibility. At the same time, PDA contains a large number of phenolic hydroxyl groups and amino groups, which provide abundant active sites for the complexation of metal ions and an excellent platform for the secondary functionalization of materials [21].

In this study, W was first modified by DA to prepare W/PDA. This is the difference between us and other researchers. Then, W/PDA/ $\text{Gd}^{3+}$  was prepared by the self-assembly method and homogeneous precipitation method. Next, W/ $\text{Gd}_2\text{O}_3$  with core-shell structure was prepared by high-temperature calcination (Figure 1). Finally, W/ $\text{Gd}_2\text{O}_3$  radiation-proof fabric was prepared by coating, and its X-ray protection and mechanical properties were studied. Section 2: “Materials and Methods” describes the preparation technology and test method of W/PDA and W/ $\text{Gd}_2\text{O}_3$ . Section 3: “Results” analyzes and discusses the data obtained from the testing of W, W/PDA, and W/ $\text{Gd}_2\text{O}_3$ . Section 4: “Conclusions” summarizes the X-ray protection efficiency and various mechanical properties of core-shell W/ $\text{Gd}_2\text{O}_3$  powder PU coating fabric.

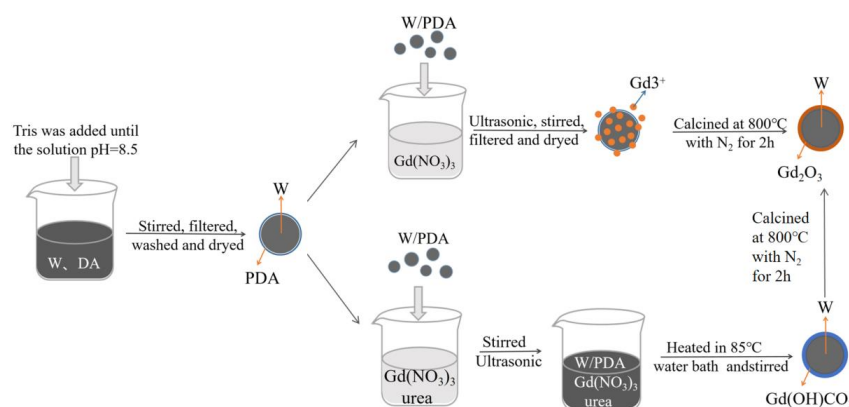


**Figure 1.** Schematic of the preparation of core-shell structure W/ $\text{Gd}_2\text{O}_3$ .

## 2. Materials and Methods

### 2.1. Materials

W powder (99.9%, 1  $\mu\text{m}$ ) was obtained from AnHui Kerun Nanotechnology Co., Ltd. (Lu'an, China). Tris (1 mol/L) and dopamine hydrochloride (98%) were obtained from Shanghai Dibai Biology Science and Technology Co., Ltd. (Shanghai, China).  $\text{Gd}(\text{NO}_3)_3 \cdot 6\text{H}_2\text{O}$  (99.99%) was obtained from Guangdong Wengjiang Chemical Reagent Co., Ltd. (Guangdong, China). Absolute ethyl alcohol ( $\geq 99.5\%$ ), urea ( $\geq 99\%$ ), and N, N-dimethylacetamide (DMAC,  $\geq 99.5\%$ ) were obtained from Shanghai Runjie Chemical Reagent Co., Ltd. (Shanghai, China). Polyurethane (PU) adhesive was obtained from Ningbo Haishu Yiduo Chemical Products Co., Ltd. (Ningbo, China).

### 2.2. Preparation and Characterization of W/PDA

(1) Explore the influence of DA solubility on coating effect. Prepare DA solutions with different concentrations (1, 1.5, 2, 2.5 g/L), add W that has been ultrasonically cleaned by ethanol, adjust the pH of the solution to 8.5 with Tris buffer, and electrically stir the mixed solution at room temperature for 16 h, filter and separate, wash it with water and ethanol twice, and then dry it.

(2) Explore the influence of stirring time on coating effect. The DA solution with concentration of 2 g/L was adjusted to pH 8.5 with Tris buffer, and W that was ultrasonically cleaned by ethanol was added. Then, the mixed solution was stirred at room temperature for different times (2, 8, 16, 24 h), filtered and separated, washed with water and ethanol twice, and then dried.

The morphology of W and W/PDA was observed by scanning electron microscopy (SEM; ZEISS Gemini SEM300, Carl Zeiss Company, Oberkochen, Germany). The elements of W/PDA were analyzed by energy dispersive spectroscopy (EDS; X-MaxN 50 mm<sup>2</sup>, Oxford Instruments company, Oxford, UK) mapping. The crystal forms of W and W/PDA were characterized by X-ray diffraction (XRD RigakuD/max-2500PC, Rigaku Company, Tokyo, Japan). The surface chemical elements and functional groups of W/PDA were characterized by X-ray photoelectron spectroscopy (XPS ESCALAB-250, Thermo Fisher Company, Waltham, MA, USA). The thermal properties of W and W/PDA were characterized by using thermogravimetric analysis (TG; TG209F3, NETZSCH, Bavaria, Germany) and the chemical structure of W/PDA was analyzed by using a Fourier transform infrared (FTIR; Thermo Nicolet iS50, Thermo Fisher Scientific shier science & technology company, Waltham, MA, USA).

### 2.3. Preparation and Characterization of W/Gd<sub>2</sub>O<sub>3</sub> by Self-Assembly Method

Prepare  $\text{Gd}(\text{NO}_3)_3$  solutions (0.1, 0.2, 0.3, 0.4 mol/L) with different concentrations, add W/PDA powder, ultrasonically disperse them for 20 min, magnetically stir for 2 h, filter, separate and dry them, and then place the prepared samples in a muffle furnace at 800 °C with  $\text{N}_2$  for 2 h (heating rate is 2 °C/min).

The morphology of W/Gd<sub>2</sub>O<sub>3</sub> was observed by SEM, and the surface chemical elements and functional groups of W/Gd<sub>2</sub>O<sub>3</sub> were characterized by XPS.

### 2.4. Preparation and Characterization of W/Gd<sub>2</sub>O<sub>3</sub> by Homogeneous Precipitation

Weigh 1.25 g of  $\text{Gd}(\text{NO}_3)_3 \cdot 6\text{H}_2\text{O}$  in a beaker, add 40 mL of deionized water, and stir with a glass rod to completely dissolve it. Then, add 4.15 g of urea and 0.5 g of W/PDA powder, stir magnetically for 30 min, and then ultrasonicate for 20 min. The ultrasonic liquid was heated in a water bath at 85 °C, magnetically stirred for 3 h, washed twice with water and ethanol, and then dried in a 60 °C oven. Finally, the dried sample was calcined in a muffle furnace at 800 °C with  $\text{N}_2$  (heating rate 2 °C/min) for 2 h [22].

The morphology of W/PDA/Gd(OH)CO<sub>3</sub> and W/Gd<sub>2</sub>O<sub>3</sub> was observed by SEM, the crystal forms of W/PDA/Gd(OH)CO<sub>3</sub> and W/Gd<sub>2</sub>O<sub>3</sub> were characterized by XRD, the thermal properties of W/PDA/Gd(OH)CO<sub>3</sub> and W/Gd<sub>2</sub>O<sub>3</sub> were characterized by TG and the chemical structure of W/PDA/Gd(OH)CO<sub>3</sub> and W/Gd<sub>2</sub>O<sub>3</sub> was analyzed by FTIR.

### 2.5. Preparation and Characterization of Radiation Protection Fabric

W/Gd<sub>2</sub>O<sub>3</sub> powder with core-shell structure and W/Gd<sub>2</sub>O<sub>3</sub> blend powder with mass ratio of 5:1 were added into DMAC for ultrasonic treatment for 30 min. After ultrasonic treatment, a certain amount of PU glue was added to ensure that the powder content in the coating was 60 wt%. Mechanical stirring was carried out for 2 h, and the uniformly stirred coating was placed into a vacuum drying oven for vacuum defoaming treatment. Fix the base cloth flat on the needle plate rack of a small coating tester, invert the prepared coating evenly at the position where the base cloth is close to the scraper, push the scraper to the other side at a constant speed, take down the whole needle plate rack, and dry it in an oven at 60 °C for 1 h.

SEM was used to observe the cross-sectional morphology of protective fabrics prepared by W and Gd<sub>2</sub>O<sub>3</sub> mixed powder and core-shell W/Gd<sub>2</sub>O<sub>3</sub> powder.

### 2.6. Radiation Protection Performance Test

An X-ray air-specific kinetic energy standard device was used to test the protective ability of radiation protective coating fabric against X-ray with reference to standard (GBZ/T 147—2002, China), and the measuring range was 1.0 × 10<sup>−5</sup> Gy/h–1.0 Gy/h. The calculation formula of protection efficiency is as follows:

$$\text{protection efficiency} = \frac{A - C}{A - B} \times 100\% \quad (1)$$

where C is the dose rate of coating fabric, A is the dose rate of uncoating fabric, and B is the background dose rate.

### 2.7. Mechanical Performance Test

**Wear resistance test:** The wear resistance of radiation protective coating fabric was tested by using the wear tester (YG(B)401T Darong textile instrument company, Wenzhou, China). According to the standard (GB/T 21196.3-2007, China), the fabric was cut into a round sample with a diameter of 38 mm, and No. 600 water sandpaper was selected as the standard abrasive. Each fabric was tested five times, and the average value was obtained. Calculate the mass loss and loss rate. The smaller the mass loss rate, the better the wear resistance. The calculation formula of the fabric mass loss rate is as follows:

$$\text{mass loss rate} = \frac{B - A}{B} \times 100\% \quad (2)$$

where B is the quality of fabric before wear, and A is the quality of the fabric after wear.

**Tensile property test:** A universal testing machine (INSTRON 1346, Instrang (Shanghai) Test Equipment Trading Co., Ltd., Shanghai, China) was used to test the breaking strength and elongation at break of radiation protective coating fabric. According to the standard (GB/T 3923.1-2013, China), the fabric was cut into strip samples with a width of 50 mm and a length of 150 mm, and each fabric was tested five times to obtain the average value.

**Tearing performance test:** the tearing strength of radiation protective coating fabric was tested by using a universal material testing machine. According to the standard (GB/T 3917.2-2009, China), the fabric was cut into strip samples with a width of 50 mm and a length of 200 mm, and then cut a slit with a length of 100 mm parallel to the length direction from the center of the width direction. Each fabric was tested five times, and the average value was taken.

## 3. Results

### 3.1. Preparation and Characterization of W/PDA

The concentration of DA is an important factor in controlling the coating rate and roughness [23]. Figure 2a shows the SEM image of metal W powder. As can be seen, the surface of W is particularly smooth. When the DA concentration is 1 g/L (Figure 2b), a small amount of PDA particles are deposited on the W surface. When the concentration of DA

increased to 1.5 g/L (Figure 2c), the PDA particles on the surface of W became more compact. When the DA concentration increased to 2 g/L (Figure 2d), W was completely covered by PDA. When the concentration of DA increased to 2.5 g/L (Figure 2e), the surface of W was covered with a thick layer of PDA, and PDA particles formed accumulation. Because the 2.5 g/L concentration of DA was too high, it was not conducive to the subsequent adsorption of  $Gd^{3+}$ . Therefore, a 2 g/L DA solution was selected to prepare W/PDA.

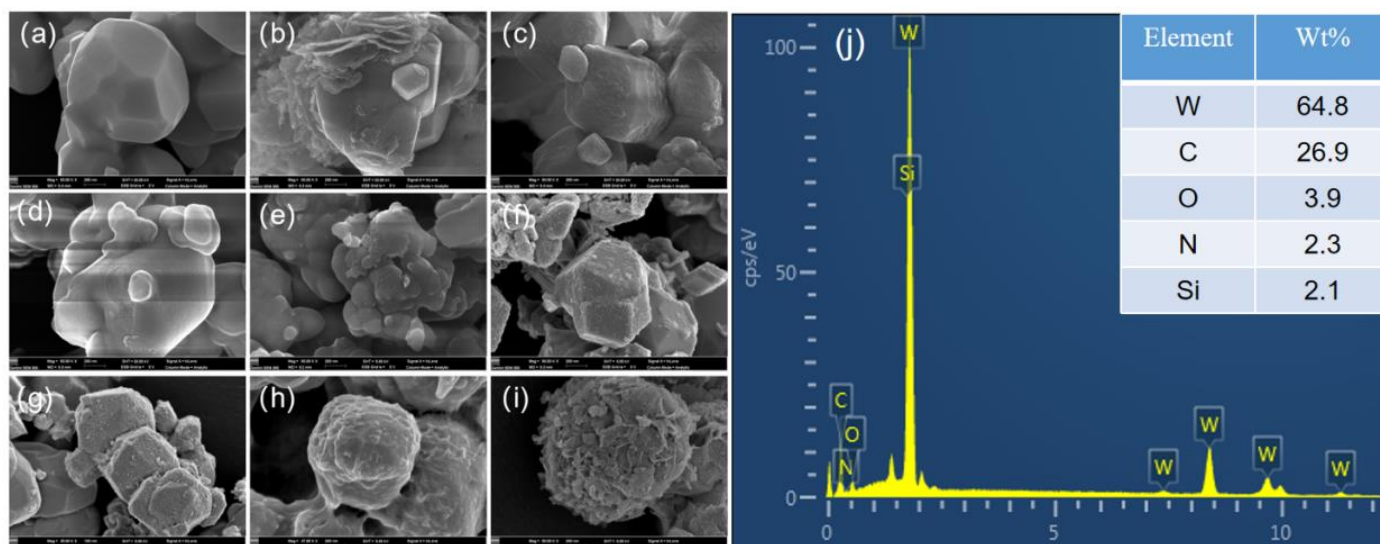


**Figure 2.** SEM: (a) pure W, (b) 1 g/L of DA to prepare W/PDA, (c) 1.5 g/L of DA to prepare W/PDA, (d) 2 g/L of DA to prepare W/PDA, (e) 2.5 g/L of DA to prepare W/PDA, (f) stirring for 2 h to prepare W/PDA, (g) stirring for 8 h to prepare W/PDA, (h) stirring for 16 h to prepare W/PDA, (i) stirring for 24 h to prepare W/PDA, (j) EDS spectra of W/PDA.

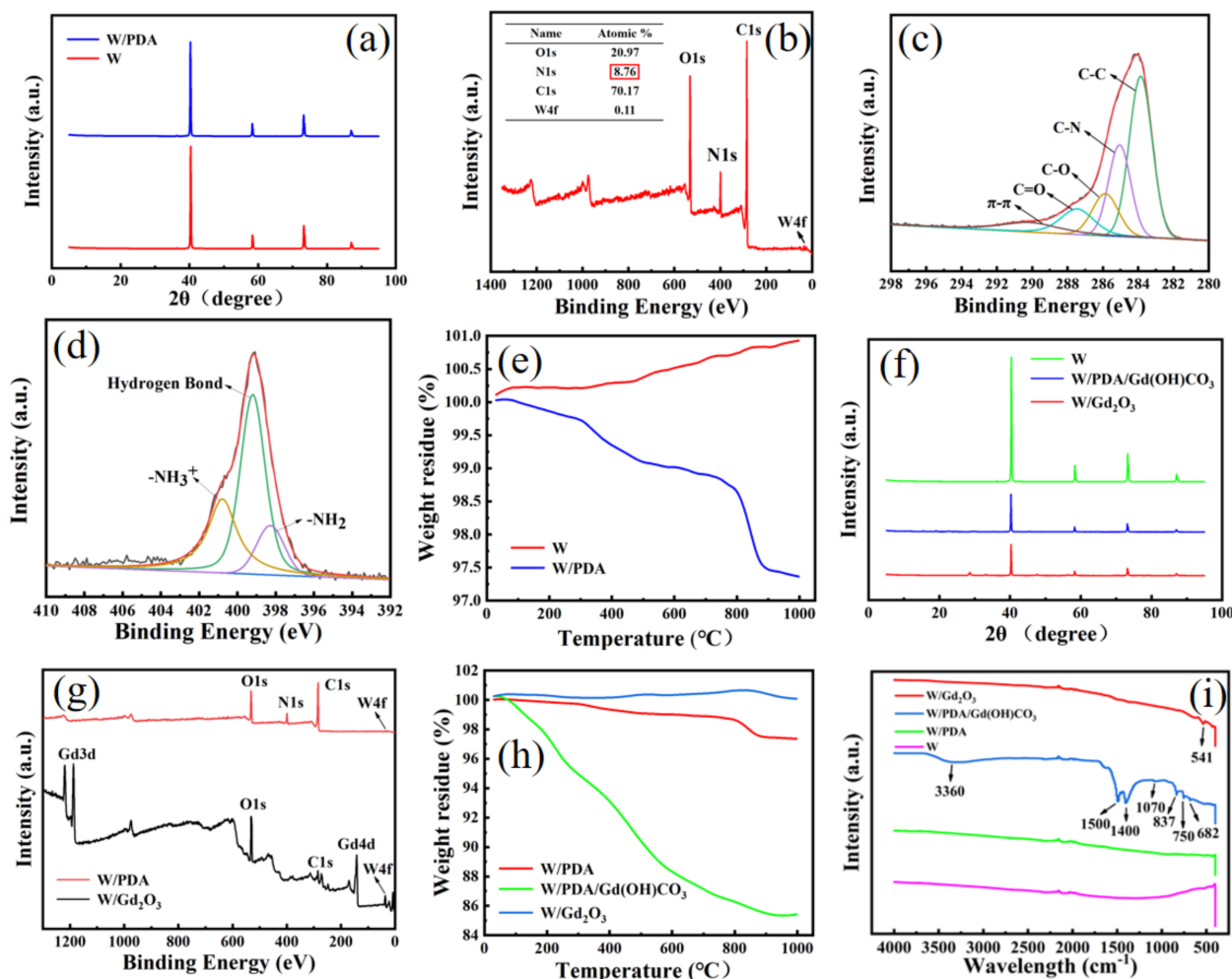
Reaction time is another important factor in controlling the coating effect. Figure 2f–i show that with the increase in reaction time, the surface of W gradually becomes rough. When the reaction time is 2 h (Figure 2f), a small amount of PDA particles are deposited on the surface of W, and the roughness is slightly increased compared with that of pure W. After the reaction time increased to 8 h (Figure 2g), the PDA particles on the surface of W increased. When the time increased to 16 h (Figure 2h), W was completely covered by PDA. When the reaction time increased to 24 h (Figure 2i), the PDA layer became thicker, the W surface was uneven, and the interface instability increased, which was not conducive to the subsequent adsorption of  $Gd^{3+}$ . Therefore, the stirring time was controlled for 16 h to prepare W/PDA.

Figure 2j is the EDS energy spectrum of W/PDA particles prepared under 2 g/L DA concentration and 16 h reaction time. The C, N, and O elements that appear are all elements that make up PDA.

Figure 3a shows the XRD patterns of pure W and W/PDA. The diffraction peak of pure W is consistent with the standard diffraction card of W (JCPDS 04-0806), and there are no other impurity peaks, which proves that the raw material is pure cubic phase W. Compared with the diffraction peak of pure W, the XRD diffraction peak of W/PDA has no change, which indicates that coating PDA has no effect on the crystal form of W.

Figure 3b–d show the XPS broad spectrum of W/PDA and the peak fitting spectra of C1s and N1s. Figure 4b shows that there are peaks of C1s, O1s, N1s, and W4f on the surface of W/PDA with molar fractions of 70.17%, 20.97%, 8.76%, and 0.11%, respectively, which are consistent with the theoretical nitrogen content of DA of 9.1%. Figure 4c is the peak spectrum of C1s, which shows that C–C (284.7 eV), C–N (285.4 eV), C–OH (287.17 eV), O=C–O (289.0 eV), and  $\pi$ – $\pi$  (291 eV) exist on the surface of W/PDA. C–N and O=C–O are the functional groups on PDA. Figure 4d shows the peak separation spectrum of N1s,

which can be simulated into peaks with bond energies of 399.08, 400.57, and 401.09 eV, respectively, corresponding to  $-\text{NH}_2$ , hydrogen bond, and  $-\text{NH}_3^+$ . Among them,  $-\text{NH}_2$  is the functional group on PDA. Combined with Figure 2d,h,j and Figure 4b–d, it can be shown that the surface of W is covered with a layer of PDA.



**Figure 3.** (a) XRD pattern of W and W/PDA; (b) XPS broad spectrum of W/PDA; (c) XPS peak fitting pattern of C1s of W/PDA; (d) XPS peak fitting pattern of N1s of W/PDA; (e) TG curve of W and W/PDA; (f) XRD pattern of W, W/PDA/Gd(OH)CO<sub>3</sub> and W/Gd<sub>2</sub>O<sub>3</sub>; (g) XPS spectra of W/PDA and W/Gd<sub>2</sub>O<sub>3</sub>; (h) TG curves of W/PDA, W/PDA/Gd(OH)CO<sub>3</sub>, and W/Gd<sub>2</sub>O<sub>3</sub>; and (i) FTIR spectra of W, W/PDA, W/PDA/Gd(OH)CO<sub>3</sub>, and W/Gd<sub>2</sub>O<sub>3</sub>.

Figure 3e shows the TG curves of W and W/PDA. The mass of W increases slightly when calcined with N<sub>2</sub> because the surface of W can adsorb a small amount of N<sub>2</sub> at a high temperature. The thermogravimetric curve of W/PDA shows that the decomposition rate of PDA accelerates with the increase in temperature, and it tends to be flat when the temperature reaches 400 °C, at which time PDA has been completely carbonized [24]. However, because PDA is carbonized into nitrogen-doped carbon spheres at a high temperature, it has a large specific surface area and pore size, and it will absorb a small amount of N<sub>2</sub> during the calcination process with N<sub>2</sub>. When the temperature is close to 800 °C, the nitrogen-doped carbon spheres collapse and release the adsorbed N<sub>2</sub>. Therefore, the weight decreased rapidly. Moreover, the weight lost by adding calcined W was the weight lost by PDA carbonization, and the weight loss rate was 2.5%, which further proved that the surface of W was successfully coated with PDA.

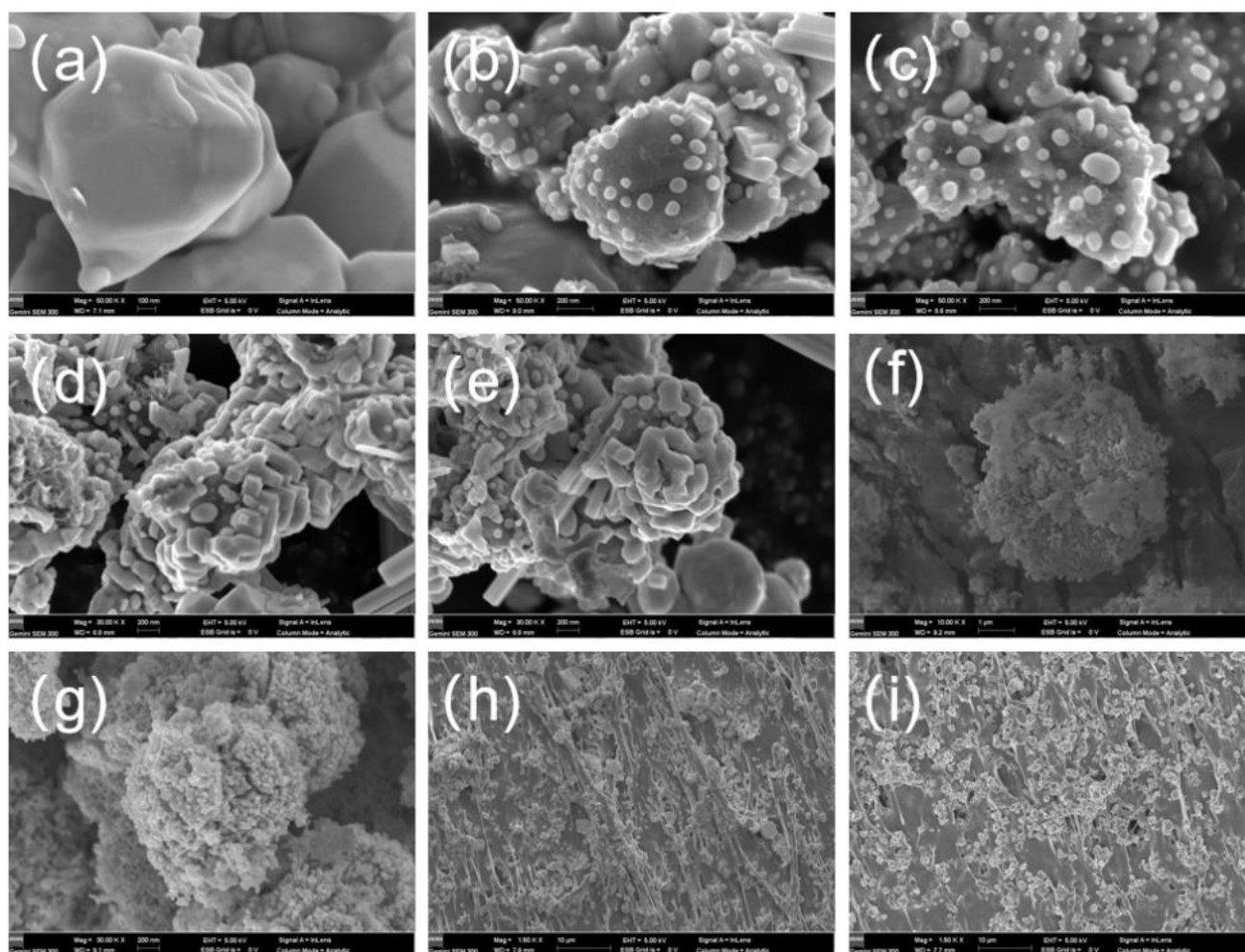


**Figure 4.** SEM images of (a) calcined W/PDA, (b) 0.1 mol/L of  $Gd^{3+}$  to prepare W/ $Gd_2O_3$ , (c) 0.2 mol/L of  $Gd^{3+}$  to prepare W/ $Gd_2O_3$ , (d) 0.3 mol/L of  $Gd^{3+}$  to prepare W/ $Gd_2O_3$ , and (e) 0.4 mol/L of  $Gd^{3+}$  to prepare W/ $Gd_2O_3$ . (f) W/PDA/GD(OH)CO<sub>3</sub>, (g) calcined product of W/PDA/GD(OH)CO<sub>3</sub>, (h) cross-sectional morphology of W/ $Gd_2O_3$  mixed powder PU coating fabric, and (i) cross-sectional morphology of core-shell structure W/ $Gd_2O_3$  powder PU coating fabric.

### 3.2. Preparation and Characterization of W/ $Gd_2O_3$ by Self-Assembly Method

Figure 4a shows the morphology of W/PDA after high-temperature calcination. As can be seen, the surface of W is smooth because PDA carbonizes after high-temperature calcination and adheres to the surface of W. The molecular chain of PDA is rich in phenolic hydroxyl and amine groups, which provide abundant active sites for the complexation of various metal ions. After calcination at a high temperature, the nitrogen-doped carbon layer is formed. When the concentration of  $Gd^{3+}$  is 0.1 mol/L (Figure 4b), the surface of W is coated with a small amount of sparse spherical  $Gd_2O_3$  particles. When the concentration of  $Gd^{3+}$  increases to 0.2 mol/L (Figure 4c), the  $Gd_2O_3$  nanoparticles on the surface of W become larger and increase in number. When the concentration of  $Gd^{3+}$  increases to 0.3 mol/L (Figure 4d), the  $Gd_2O_3$  nanoparticles on the W surface combine with each other to form the core-shell structure of W/ $Gd_2O_3$ . This is because  $Gd_2O_3$  nanoparticles combine with each other to form larger  $Gd_2O_3$  particles with the increase in  $Gd^{3+}$  concentration. After increasing the concentration of  $Gd^{3+}$  to 0.4 mol/L (Figure 4e), the  $Gd_2O_3$  nanoparticles on the W surface have little change compared with that when the concentration of  $Gd^{3+}$  is 0.3 mol/L. This is because the chelation of PDA on the W surface to  $Gd^{3+}$  has reached saturation when the concentration of  $Gd^{3+}$  is 0.3 mol/L [25]. Therefore, the concentration of  $Gd^{3+}$  used to prepare W/ $Gd_2O_3$  was set to 0.3 mol/L.

Figure 3g is the XPS full spectrum of W/PDA and W/Gd<sub>2</sub>O<sub>3</sub>. Compared with W/PDA, the peak of C1s in the XPS spectrum of W/Gd<sub>2</sub>O<sub>3</sub> decreases, and the peak of O1s increases. This is because PDA on the surface of the sample adsorbed Gd<sup>3+</sup> and then cracked into nitrogen-doped carbon and Gd<sub>2</sub>O<sub>3</sub> at a high temperature. The absorption peaks of Gd4d, O1s, and Gd3d appear at 143.08, 531.08, and 1188.08 eV, and the chemical bond of Gd<sub>2</sub>O<sub>3</sub> is at 531.08 eV [26], which proves that the surface of W is coated with a layer of Gd<sub>2</sub>O<sub>3</sub> shell structure.

### 3.3. Preparation and Characterization of W/Gd<sub>2</sub>O<sub>3</sub> by Homogeneous Precipitation

Figure 4f is the SEM image of Gd(OH)CO<sub>3</sub> deposited on the W/PDA surface. When the reaction temperature exceeds 70 °C, urea begins to decompose to generate CO<sub>3</sub><sup>2-</sup> ions, and CO<sub>3</sub><sup>2-</sup> reacts with hydrolyzed Gd<sup>3+</sup> to generate Gd(OH)CO<sub>3</sub>, which is deposited on the surface of W/PDA [27]. With the progress of the reaction, Gd(OH)CO<sub>3</sub> continued to grow and finally completely covered the surface of W/PDA, resulting in W/PDA/Gd(OH)CO<sub>3</sub> composite microspheres [28]. Figure 4g shows the calcined product of W/PDA/Gd(OH)CO<sub>3</sub>. As can be seen, the surface of the sample is coated with dense nanoparticles, which is because the loosely arranged precursor Gd(OH)CO<sub>3</sub> particles are converted into Gd<sub>2</sub>O<sub>3</sub> after being calcined at a high temperature.

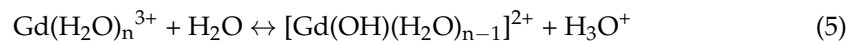
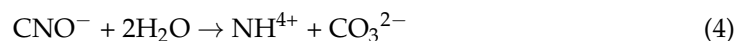


Figure 3f shows the XRD patterns of W, W/PDA/Gd(OH)CO<sub>3</sub>, and W/Gd<sub>2</sub>O<sub>3</sub>. The diffraction peak of W/PDA/Gd(OH)CO<sub>3</sub> is consistent with W, and no other impurity peaks appear, indicating that the precursor Gd(OH)CO<sub>3</sub> is amorphous. However, W/Gd<sub>2</sub>O<sub>3</sub> has diffraction peaks other than W, and there are (222), (400), (440), and (622) planes of cubic Gd<sub>2</sub>O<sub>3</sub> at 2θ = 28.62, 33.15, 47.56, and 56.58, but there are no other impurity peaks, which is consistent with the standard diffraction card of Gd<sub>2</sub>O<sub>3</sub> (JCPDS 88-2165). This indicates that the surface of W was successfully coated with pure cubic Gd<sub>2</sub>O<sub>3</sub>.

Figure 3h shows the TG curves of W/PDA, W/PDA/Gd(OH)CO<sub>3</sub>, and W/Gd<sub>2</sub>O<sub>3</sub>. With the increase in temperature, PDA loses weight when carbonized at a high temperature, and the weight loss rate is 2.5%. The thermogravimetric curve of precursor W/PDA/Gd(OH)CO<sub>3</sub> shows that the total weight loss rate is 15% in the whole thermal decomposition process, and the weight loss of Gd(OH)CO<sub>3</sub> is 12.5%. The thermal decomposition process of Gd(OH)CO<sub>3</sub> can be divided into two stages. The first stage is when Gd(OH)CO<sub>3</sub> loses one molecule of H<sub>2</sub>O and one molecule of CO<sub>2</sub>, thus transforming Gd<sub>2</sub>OCO<sub>3</sub>. When the temperature reaches 560 °C, Gd<sub>2</sub>OCO<sub>3</sub> loses one molecule of CO<sub>2</sub> and then changes into Gd<sub>2</sub>O<sub>3</sub>. The thermal weight loss curve and weight loss rate of Gd<sub>2</sub>O<sub>3</sub> approach zero, which proves that the precursor Gd(OH)CO<sub>3</sub> has been completely converted into Gd<sub>2</sub>O<sub>3</sub> after calcination at 800 °C.

Figure 3i shows the infrared absorption spectra of W, W/PDA, W/PDA/Gd(OH)CO<sub>3</sub>, and W/Gd<sub>2</sub>O<sub>3</sub>. Compared with pure W powder, there is no new absorption peak in the infrared spectrum of W/PDA, which indicates that there is no new chemical bond between W powder and PDA. Compared with W/PDA, the precursor W/PDA/Gd(OH)CO<sub>3</sub> has a strong absorption peak at 1400 and 1500 cm<sup>-1</sup>, a weak absorption peak at 1070 cm<sup>-1</sup>, a moderate absorption peak at 837 cm<sup>-1</sup>, and absorption peaks at 682 and 750 cm<sup>-1</sup>. The combination of these absorption bands indicates the formation of Gd(OH)CO<sub>3</sub>, and the absorption peak of W/PDA/Gd(OH)CO<sub>3</sub> near 3360 cm<sup>-1</sup> is the absorption peak of O-H in water molecules adsorbed on Gd(OH)CO<sub>3</sub>. Compared with W/PDA/Gd(OH)CO<sub>3</sub>, the characteristic peaks of W/PDA/Gd(OH)CO<sub>3</sub> in the infrared absorption spectrum of W/Gd<sub>2</sub>O<sub>3</sub> disappeared, and the Gd-O vibration absorption peak of Gd<sub>2</sub>O<sub>3</sub> appeared at

$541 \text{ cm}^{-1}$ . This shows that the precursor  $\text{Gd}(\text{OH})\text{CO}_3$  can be completely converted into core-shell  $\text{Gd}_2\text{O}_3$  [29] by calcination at  $800 \text{ }^\circ\text{C}$ .

#### 3.4. Preparation and Characterization of Radiation Protection Fabric

Because of the strong penetration of X-rays, the high-density plate or sheet composed of heavy metals has a good protective effect, but it cannot be applied to protective clothing because of its poor wearability. PU resin-coating fabric has excellent wearability and mechanical properties, and the most important factor affecting its X-ray protection performance is the protection performance and quantity distribution of heavy metal or metal oxide powder in PU resin coating. Figure 4h shows the cross-section of the radiation protection PU coating fabric of W and  $\text{Gd}_2\text{O}_3$  mixed powder, and Figure 4i shows the cross-section of the core-shell structure W/ $\text{Gd}_2\text{O}_3$  radiation protection PU coating fabric. The powder addition of the two PU coating fabrics is 60 wt%, and both of them have good dispersibility in PU resin. The interface effect between W/ $\text{Gd}_2\text{O}_3$  and PU resin is better because compared with inorganic metals, the PDA on the surface of core-shell structure W/ $\text{Gd}_2\text{O}_3$  is carbonized at high temperature to form nitrogen-doped carbon, which has strong hydrophilicity. The particles in the coatings of the two PU coating protective fabrics are closely linked, seamless and layered, and close to continuous distribution, which proves that a dense radiation shielding layer can be formed.

#### 3.5. Radiation Protection Performance Test

Figure 5a,b show the protective performance of PU coating fabric with W and  $\text{Gd}_2\text{O}_3$  mixed powder and core-shell structure W/ $\text{Gd}_2\text{O}_3$  powder, respectively. Compared with W and  $\text{Gd}_2\text{O}_3$  mixed powder PU coating fabric, the protective efficiency and lead equivalent of W/ $\text{Gd}_2\text{O}_3$  powder PU coating fabric with core-shell structure for different energy ray protection are obviously improved. With the increase in incident energy, the protective efficiency of core-shell structure W/ $\text{Gd}_2\text{O}_3$  powder PU coating fabric decreases more slowly than that of W/ $\text{Gd}_2\text{O}_3$  mixed powder PU coating fabric. This is because the secondary radiation generated by the protective material while absorbing X-rays can be better absorbed again in the core-shell structure. The weak absorption areas of W and  $\text{Gd}_2\text{O}_3$  are 90.5 and 50.2 keV, respectively. When the incident energy is 65–100 keV, the protective efficiency of core-shell structure W/ $\text{Gd}_2\text{O}_3$  powder PU coating fabric is above 60%, showing a good synergistic protective effect. When the incident energy is 83 keV, the X-ray protection efficiency of core-shell W/ $\text{Gd}_2\text{O}_3$  powder PU coating fabric is 65.5%, and the lead equivalent is 0.4051 mmPb.

#### 3.6. Mechanical Performance Test

More than 70% of fabric damage is caused by wear, so wear resistance is a very important performance index of fabric. Figure 5d shows the mass loss rate of pure PU coating fabric, W and  $\text{Gd}_2\text{O}_3$  mixed powder PU coating fabric, and core-shell structure W/ $\text{Gd}_2\text{O}_3$  powder PU coating fabric after 10,000 rubs. Comparing the pure PU coating fabric with the coating fabric after adding shielding powder into PU resin, the wear resistance of PU coating fabric with shielding powder decreases. This is mainly because adding shielding powder into the resin will form gaps in the resin, thus reducing the fastness of the resin. However, the reduction range is very small, so the addition of shielding powder has little effect on the wear resistance of the fabric. Comparing W and  $\text{Gd}_2\text{O}_3$  mixed powder PU coating fabric with core-shell structure W/ $\text{Gd}_2\text{O}_3$  powder PU coating fabric, the PU coating fabric with core-shell structure W/ $\text{Gd}_2\text{O}_3$  powder has better wear resistance. This may be because the particle size of core-shell structure W/ $\text{Gd}_2\text{O}_3$  is relatively uniform, and the gaps in the resin are less and uniform, so the wear resistance is better.

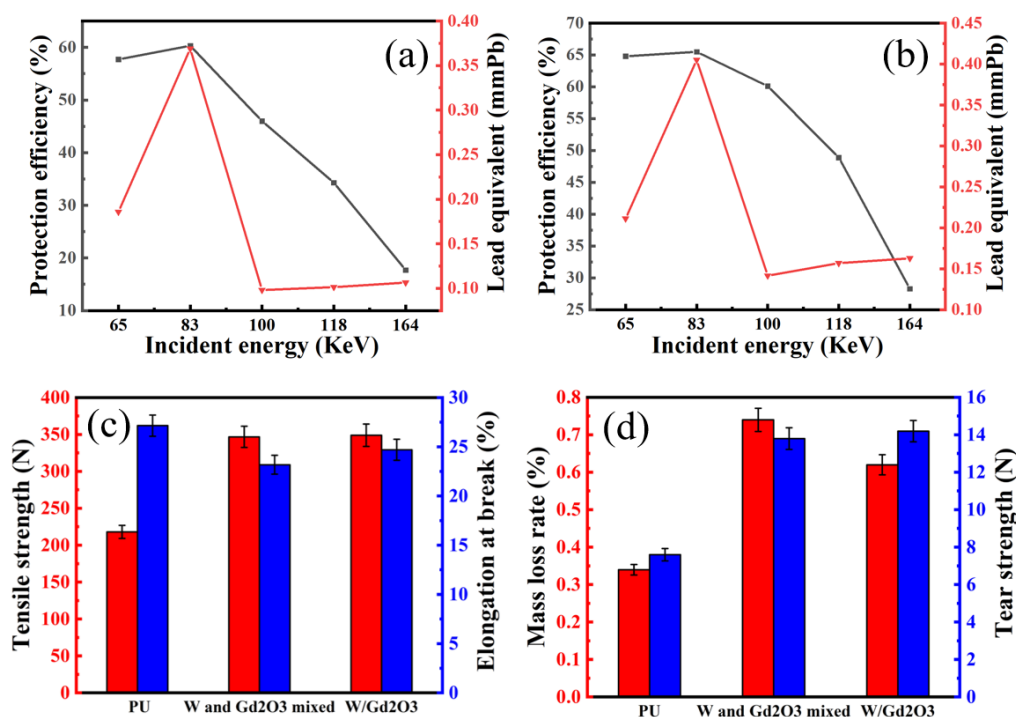


**Figure 5.** (a) Protective performance of PU coating fabric with W and Gd<sub>2</sub>O<sub>3</sub> mixed powder; (b) protective performance of PU coating fabric with core-shell structure W/Gd<sub>2</sub>O<sub>3</sub> powder; (c) tensile properties of pure PU coating fabric, W and Gd<sub>2</sub>O<sub>3</sub> mixed powder PU coating fabric, and core-shell structure W/Gd<sub>2</sub>O<sub>3</sub> powder PU coating fabric; (d) Wear resistance and tearing properties of pure PU coating fabric, W and Gd<sub>2</sub>O<sub>3</sub> mixed powder PU coating fabric and core-shell structure W/Gd<sub>2</sub>O<sub>3</sub> powder PU coating fabric.

Figure 5c shows the test results of breaking strength and elongation at break of pure PU coating fabric, W and Gd<sub>2</sub>O<sub>3</sub> mixed powder PU coating fabric, and core-shell structure W/Gd<sub>2</sub>O<sub>3</sub> powder PU coating fabric. Compared with pure PU coating fabrics, two kinds of PU coating fabrics with shielding powder have higher breaking strength and lower elongation at break. This is because the metal powder has a certain rigidity, which can prevent the dislocation of polymer lattice during the fabric stretching process, thus improving the breaking strength of the coating fabric. However, the addition of shielding powder decreases the elongation at the break of the fabric. This is because the addition of shielding powder will reduce the amount of resin, and the metal powder will create gaps between the resins, thus reducing the tensile elasticity of the coating fabric.

Figure 5d shows the test results of tear strength of pure PU coating fabric, W and Gd<sub>2</sub>O<sub>3</sub> mixed powder PU coating fabric, and core-shell structure W/Gd<sub>2</sub>O<sub>3</sub> powder PU coating fabric. Comparing pure PU coating fabric with a coating fabric with inorganic metal powder, the addition of powder enhances the tearing strength of the fabric, which is mainly due to the fact that the metal powder itself has a certain rigidity and can prevent the dislocation of polymer lattice in the tearing process, thus improving the tearing strength of the coating fabric. Figure 4d shows the test results of tear strength of pure PU coating fabric, W and Gd<sub>2</sub>O<sub>3</sub> mixed powder PU coating fabric, and core-shell structure W/Gd<sub>2</sub>O<sub>3</sub> powder PU coating fabric. Comparing pure PU coating fabric with a coating fabric with inorganic metal powder, the addition of powder enhances the tearing strength of the fabric, which is mainly due to the fact that the metal powder itself has a certain rigidity and can prevent the dislocation of polymer lattice in the tearing process, thus improving the tearing strength of the coating fabric.

#### 4. Conclusions

W powder was added into 2 g/L DA solution and mechanically stirred for 16 h, and W/PDA was successfully prepared. W/Gd<sub>2</sub>O<sub>3</sub> with core-shell structure was prepared by self-assembly method and homogeneous precipitation method. At the same time, PU coating fabrics with W and Gd<sub>2</sub>O<sub>3</sub> mixed powder and core-shell structure W/Gd<sub>2</sub>O<sub>3</sub> powder were prepared, and their X-ray protection performance was tested. The results showed that compared with W and Gd<sub>2</sub>O<sub>3</sub> mixed powder PU coating fabrics, the protection efficiency and lead equivalent of core-shell structure W/Gd<sub>2</sub>O<sub>3</sub> powder PU coating fabrics for different energy ray protection were obviously improved. With the increase in incident energy, the protective efficiency of core-shell structure W/Gd<sub>2</sub>O<sub>3</sub> powder PU coating fabric decreases more slowly than that of W/Gd<sub>2</sub>O<sub>3</sub> mixed powder PU coating fabric. When the incident energy is 65–100 keV, the protective efficiency of the core-shell structure W/Gd<sub>2</sub>O<sub>3</sub> powder PU coating fabric is above 60%, showing a good synergistic protective effect. When the incident energy is 83 keV, the X-ray protection efficiency of core-shell W/Gd<sub>2</sub>O<sub>3</sub> powder PU coating fabric is 65.5%, and the lead equivalent is 0.4051 mmPb. Therefore, the preparation of the core-shell structure radiation-proof material with heavy metals or metal oxides in different weak protection areas can effectively improve the X-ray protection performance of the material itself and can re-absorb the secondary radiation generated in the radiation absorption process. In addition, in terms of mechanical properties, the breaking strength, elongation at break, the wear resistance, and tearing strength of pure PU-coated fabric, W, and Gd<sub>2</sub>O<sub>3</sub> mixed powder PU-coated fabric, and core-shell structure W/Gd<sub>2</sub>O<sub>3</sub> powder PU-coated fabric were measured. Compared with pure PU-coated fabrics, the core-shell structure W/Gd<sub>2</sub>O<sub>3</sub> powder PU-coated fabrics have higher breaking strength, lower elongation at break, lower wear resistance, and higher tearing strength.

**Author Contributions:** Conceptualization, L.Y.; methodology, L.Y.; software, S.X.; validation, Y.X., T.Y. and L.Y.; formal analysis, Y.X.; investigation, Y.X.; resources, G.P.; data curation, G.P.; writing—original draft preparation, Y.X. and T.Y.; writing—review and editing, S.X.; visualization, G.P.; supervision, S.X.; project administration, G.P.; funding acquisition, L.Y. All authors have read and agreed to the published version of the manuscript.

**Funding:** This research was funded by the National Key Research and Development Program of China, grant number (2018YFC0810301) and Major Projects of Basic Science in Colleges and Universities in Jiangsu (21KJA490001).

**Institutional Review Board Statement:** Not applicable.

**Informed Consent Statement:** Not applicable.

**Data Availability Statement:** The data that support the findings of this study are available from the corresponding author upon reasonable request.

**Conflicts of Interest:** The authors declare no conflict of interest.

#### References

1. Daniele, G. Individual Radiation Protection: Idea and Research Needs. *J. Radiol. Prot.* **2019**, *39*, 641–646. [[CrossRef](#)]
2. Reading, R. Radiation exposure from CT scans in childhood and subsequent risk of leukaemia and brain tumours: A retrospective cohort study. *Child Care Health Dev.* **2012**, *38*, 910. [[CrossRef](#)]
3. Boaira, M.S.; Chaffey, C.E. Effects of coupling agents on the mechanical and rheological properties and mica-reinforced polypropylene. *Polym. Eng. Sci.* **1977**, *17*, 715–718. [[CrossRef](#)]
4. Bibbo, G. Shielding of medical imaging X-ray facilities: A simple and practical method. *Australas. Phys. Eng. Sci. Med.* **2017**, *40*, 925–930. [[CrossRef](#)]
5. Fan, G.; Geng, L.; Wang, G.; Zheng, Z. A novel radiation protection material: BaPbO<sub>3</sub>/Al composite. *Mater. Des.* **2009**, *30*, 862–866. [[CrossRef](#)]
6. Spillantini, P.; Casolino, M.; Durante, M. Shielding from cosmic radiation for interplanetary missions: Active and passive methods. *Radiat. Meas.* **2009**, *42*, 14–23. [[CrossRef](#)]
7. Nuñez-Briones, A.G.; Benavides, R.; Mendoza-Mendoza, E.; Martínez-Pardo, M.E.; Carrasco-Abrego, H.; Kotzian, C.; Saucedo-Zendejo, F.R.; García-Cerda, L.A. Preparation of PVC/Bi<sub>2</sub>O<sub>3</sub> composites and their evaluation as low energy X-ray radiation shielding. *Radiat. Phys. Chem.* **2021**, *179*, 109198. [[CrossRef](#)]

8. Cherkashina, N.I.; Pavlenko, V.I.; Noskov, A.V. Radiation shielding properties of polyimide composite materials. *Radiat. Phys. Chem.* **2019**, *159*, 111–117. [[CrossRef](#)]
9. Kijima, K.; Krisanachinda, A.; Pasawang, P.; Hanaoka, K.; Nishimura, Y. Shielding Efficiency of Novel Tungsten Rubber against Radionuclides of <sup>99m</sup>Tc, <sup>131</sup>I, <sup>18</sup>F and <sup>68</sup>Ga. *Radiat. Phys. Chem.* **2020**, *172*, 108755. [[CrossRef](#)]
10. Bilous, V.A.; Borysenko, V.M.; Voevodin, V.M.; Didenko, S.Y.; Chenko, M.I.; Neklyudov, I.M.; Rybka, O.V. Dependence of the Radiation-Protective Efficiency of AL-PB Multilayer Composites on Their Structure. *Mater. Sci.* **2015**, *50*, 600–603. [[CrossRef](#)]
11. Kim, H.; Lim, J.; Kim, J.; Lee, J.; Seo, Y. Multilayer Structuring of Nonlead Metal (BiSn)/Polymer/Tungsten Composites for Enhanced  $\gamma$ -Ray Shielding. *Adv. Eng. Mater.* **2020**, *22*, 1901448. [[CrossRef](#)]
12. Sun, Y.; Zhang, L.; Wang, Y.; Chen, P.; Xin, S.; Jiu, H.; Liu, J. Hollow and Hollow Core/shell CeO<sub>2</sub>/SiO<sub>2</sub>@CeO<sub>2</sub> Spheres: Synthesis, Structure Evolution and Catalytic Properties. *J. Alloys Compd.* **2014**, *586*, 441–447. [[CrossRef](#)]
13. Zhou, J.; Ao, J.; Xia, Y.; Xiong, H. Stable photoluminescent ZnO@Cd(OH)<sub>2</sub> core-shell nanoparticles synthesized via ultrasonication-assisted sol-gel method. *J. Colloid Interface Sci.* **2013**, *393*, 80–86. [[CrossRef](#)] [[PubMed](#)]
14. Soylu, H.M.; Lambrecht, F.Y.; Ersöz, O.A. Gamma radiation shielding efficiency of a new lead-free composite material. *J. Radioanal. Nucl. Chem.* **2015**, *305*, 529–534. [[CrossRef](#)]
15. Shang, W.; Meng, H.; Wen, Y. Influence of preparation temperature on the electrochemical characteristics of the Dodecafluoroheptyl-propyl-trimethoxysilane SAMs on aluminum alloy 6061. *Surf. Coat. Technol.* **2014**, *258*, 574–579. [[CrossRef](#)]
16. Ciliberto, E.; Condorelli, G.G.; Delfa, S.L.; Viscuso, E. Nanoparticles of Sr(OH)<sub>2</sub>: Synthesis in homogeneous phase at low temperature and application for cultural heritage artefacts. *Appl. Phys. A* **2008**, *92*, 137–141. [[CrossRef](#)]
17. Huang, Y.; Zhang, W.; Liang, L.; Xu, J.; Chen, Z. A “Sandwich” type of neutron shielding composite filled with boron carbide reinforced by carbon fiber. *Chem. Eng. J.* **2013**, *220*, 143–150. [[CrossRef](#)]
18. Yin, J.; Chen, D.; Zhang, Y.; Li, C.; Liu, L.; Shao, Y. MRI relaxivity enhancement of gadolinium oxide nanoshells with a controllable shell thickness. *Phys. Chem. Chem. Phys.* **2018**, *20*, 10038–10047. [[CrossRef](#)]
19. Li, W.; Zheng, X.; Li, F.; Wang, J. Facile Synthetic Route to Hollow Gadolinium Oxide Spheres with Tunable Thickness. *Micro Nano Lett.* **2012**, *7*, 1267–1269. [[CrossRef](#)]
20. Lee, H.; Dellatore, S.M.; Miller, W.M.; Messersmith, P.B. Mussel-Inspired Surface Chemistry for Multifunctional Coatings. *Science* **2007**, *318*, 426–430. [[CrossRef](#)]
21. Lee, H.; Rho, J.; Messersmith, P.B. Facile Conjugation of Biomolecules onto Surfaces via Mussel Adhesive Protein Inspired Coatings. *Adv. Mater.* **2009**, *21*, 431–434. [[CrossRef](#)] [[PubMed](#)]
22. Jia, G.; You, H.P.; Liu, K.; Zheng, Y.H.; Guo, N.; Zhang, H.J. Highly uniform Gd<sub>2</sub>O<sub>3</sub> hollow microspheres: Template-directed synthesis and luminescence properties. *Langmuir ACS J. Surf. Colloids* **2010**, *26*, 5122–5128. [[CrossRef](#)] [[PubMed](#)]
23. Liu, X.; Cao, J.; Li, H.; Li, L.; Jin, Q.; Ren, K.; Ji, J. Mussel-inspired polydopamine: A biocompatible and ultrastable coating for nanoparticles in vivo. *ACS Nano* **2013**, *7*, 9384–9395. [[CrossRef](#)] [[PubMed](#)]
24. Xu, C.; Tian, M.; Liu, L. Fabrication and Properties of Silverized Glass Fiber by Dopamine Functionalization and Electroless Plating. *J. Electrochem. Soc.* **2012**, *159*, 1945–7111. [[CrossRef](#)]
25. Wang, Z.; Xie, Y.; Li, Y.; Huang, Y.; Parent, L.R.; Ditri, T.; Zang, N.; Rinehart, J.D.; Gianneschi, N.C. Tunable, metal-loaded polydopamine nanoparticles analyzed by magnetometry. *Chem. Mater.* **2017**, *29*, 8195–8201. [[CrossRef](#)]
26. Kong, J.; Yee, W.A.; Yang, L.; Wei, Y.; Phua, S.L.; Ong, H.G.; Ang, J.M.; Li, X.; Lu, X. Highly electrically conductive layered carbon derived from polydopamine and its functions in SnO<sub>2</sub>-based lithium ion battery anodes. *Chem. Commun.* **2012**, *48*, 10316. [[CrossRef](#)]
27. Khakzadian, J.; Hosseini, H.R.M.; Bagherzadeh, E. A three-layered multifunctional photoactive core-shell gadolinium based nanocomposite. *Ceram. Int.* **2019**, *45*, 21228–21234. [[CrossRef](#)]
28. Kim, J.H.; Yun, K.J.; Lee, J.K. Synthesis and characterization of hollow nanoparticles of crystalline Gd<sub>2</sub>O<sub>3</sub>. *J. Nanopart. Res.* **2011**, *13*, 2311–2318. [[CrossRef](#)]
29. Liu, G.; Hong, G.; Wang, J.; Dong, X. Hydrothermal synthesis of spherical and hollow Gd<sub>2</sub>O<sub>3</sub>: Eu<sup>3+</sup> phosphors. *J. Alloys Compd.* **2006**, *432*, 200–204. [[CrossRef](#)]